

accepted for ApJ

Particle Acceleration and Magnetic Field Generation in Electron-Positron Relativistic Shocks

K.-I. Nishikawa¹

National Space Science and Technology Center, Huntsville, AL 35805

ken-ichi.nishikawa@nssstc.nasa.gov

P. Hardee

Department of Physics and Astronomy, The University of Alabama, Tuscaloosa, AL 35487

hardee@athena.astr.ua.edu

G. Richardson

*Department of Mechanical and Aerospace Engineering University of Alabama in Huntsville
Huntsville, AL 35899*

georgia.richardson@msfc.nasa.gov

R. Preece

*Department of Physics, University of Alabama in Huntsville, Huntsville, AL 35899 and
National Space Science and Technology Center, Huntsville, AL 35805*

H. Sol

LUTH, Observatoire de Paris-Meudon, 5 place Jules Jansen 92195 Meudon Cedex, France

and

G. J. Fishman

*NASA-Marshall Space Flight Center,
National Space Science and Technology Center, Huntsville, AL 35805*

¹NRC Associate / NASA Marshall Space Flight Center

ABSTRACT

Shock acceleration is an ubiquitous phenomenon in astrophysical plasmas. Plasma waves and their associated instabilities (e.g., Buneman, Weibel and other two-stream instabilities) created in collisionless shocks are responsible for particle (electron, positron, and ion) acceleration. Using a 3-D relativistic electromagnetic particle (REMP) code, we have investigated particle acceleration associated with a relativistic electron-positron jet front propagating into an ambient electron-positron plasma with and without initial magnetic fields. We find small differences in the results for no ambient and modest ambient magnetic fields. New simulations show that the Weibel instability created in the collisionless shock front accelerates jet and ambient particles both perpendicular and parallel to the jet propagation direction. Furthermore, the non-linear fluctuation amplitudes of densities, currents, electric, and magnetic fields in the electron-positron shock are larger than those found in the electron-ion shock studied in a previous paper at the comparable simulation time. This comes from the fact that both electrons and positrons contribute to generation of the Weibel instability. Additionally, we have performed simulations with different electron skin depths. We find that growth times scale inversely with the plasma frequency, and the sizes of structures created by the Weibel instability scale proportional to the electron skin depth. This is the expected result and indicates that the simulations have sufficient grid resolution. While some Fermi acceleration may occur at the jet front, the majority of electron and positron acceleration takes place behind the jet front and cannot be characterized as Fermi acceleration. The simulation results show that the Weibel instability is responsible for generating and amplifying nonuniform, small-scale magnetic fields which contribute to the electron's (positron's) transverse deflection behind the jet head. This small scale magnetic field structure is appropriate to the generation of "jitter" radiation from deflected electrons (positrons) as opposed to synchrotron radiation. The jitter radiation has different properties than synchrotron radiation calculated assuming a uniform magnetic field. The jitter radiation resulting from small scale magnetic field structures may be important for understanding the complex time structure and spectral evolution observed in gamma-ray bursts or other astrophysical sources containing relativistic jets and relativistic collisionless shocks.

Subject headings: relativistic jets: Weibel instability - shock formation - electron-positron plasma, particle acceleration - particle-in-call

1. Introduction

Nonthermal radiation observed from astrophysical systems containing relativistic jets and shocks, e.g., active galactic nuclei (AGNs), gamma-ray bursts (GRBs), and Galactic microquasar systems usually has power-law emission spectra. In most of these systems, the emission is thought to be generated by accelerated electrons through the synchrotron and/or inverse Compton mechanisms. Radiation from these systems is observed in the radio through the gamma-ray region. Radiation in optical and higher frequencies typically requires particle acceleration in order to counter radiative losses. It has been proposed that the needed particle acceleration occurs in shocks produced by differences in flow speed.

Fermi acceleration is the most widely known mechanism for the acceleration of particles in astrophysical environments characterized by a power-law spectrum. This mechanism for particle acceleration relies on the shock jump conditions in relativistic shocks (e.g., Gallant 2002; Niemiec & Oskowski 2004). Most astrophysical shocks are collisionless since dissipation is dominated by wave-particle interactions rather than particle-particle collisions. Diffusive shock acceleration (DSA) relies on repeated scattering of charged particles by magnetic irregularities (Alfvén waves) to confine the particles near the shocks. However, particle acceleration near relativistic shocks cannot be characterized as DSA because the propagation of accelerated particles ahead of the shock cannot be described by spatial diffusion. Anisotropies in the angular distribution of the accelerated particles are large, and the diffusion approximation for spatial transport does not apply (Achterberg et al. 2001).

Previous microphysical analyses of the energy conversion in relativistic pair outflows interacting with an interstellar medium consisting of cold protons and electrons (e.g., Brainerd 2000; Schlickeiser et al. 2002) have demonstrated that the beam excites both electrostatic and low-frequency magnetohydrodynamic Alfvén-type waves via a two-stream instability in the background plasma. This work has also provided the time evolution of the distribution functions of beam particles and the generated plasma wave turbulence power spectra. While in these simulations the jet front showed some evidence of Fermi acceleration, the main acceleration of electrons appeared to take place in the downstream region (e.g., Brainerd 2000; Schlickeiser et al. 2002; Ostrowski & Bednarz 2002). Further work in this area is required if significant progress is to be made in unraveling the important collisionless processes in relativistic shocks.

Particle-in-cell (PIC) simulations can shed light on the physical mechanism of particle acceleration that occurs in the complicated dynamics within relativistic shocks. Recent PIC simulations using injected relativistic electron-ion jets show that acceleration occurs within the downstream jet, rather than by the scattering of particles back and forth across the shock as in Fermi acceleration (Frederiksen et al. 2003, 2004; Nishikawa et al. 2003),

and Silva et al. (2003) have presented simulations of the collision of two inter-penetrating electron-positron plasma shells as a model of an astrophysical collisionless shock. In the electron-positron simulations performed with counter-streaming jets (Silva et al. 2003), shock dynamics involving the propagating jet head (where Fermi acceleration may take place) was not investigated. In general, these independent simulations have confirmed that relativistic jets excite the Weibel instability (Weibel 1959). The Weibel instability generates current filaments and associated magnetic fields (Medvedev & Loeb 1999; Brainerd 2000; Pruet et al. 2001; Gruzinov 2001), and accelerates electrons (Silva et al. 2003; Frederiksen et al. 2003, 2004; Nishikawa et al. 2003).

In this paper we present new simulation results of particle acceleration and magnetic field generation for relativistic electron-positron shocks using 3-D relativistic electromagnetic particle-in-cell (REMP) simulations. These new simulation results are compared to previous electron-ion results. In our new simulations, an electron-positron relativistic jet with Lorentz factor, $\gamma = 5$ (corresponds to 2.5 MeV) is injected into an electron-positron plasma in order to study the dynamics of a relativistic collisionless shock both with and without an initial ambient magnetic field. This particular choice of Lorentz factor is appropriate to the production of an internal jet shock in AGN jets or GRB jets when the high speed material has a Lorentz factor about ten times the Lorentz factor of the low speed material.

In the collisionless shock generated behind the head of the relativistic jet the Weibel instability is excited in the downstream region. The instability generates current filaments elongated along the streaming direction and associated transverse magnetic fields. Acceleration of electrons and positrons in the jet and ambient plasma accompanies the development of the Weibel instability. In §2 the simulation model and initial conditions are described. The simulation results including comparisons with previous electron-ion simulations (Nishikawa et al. 2003, hereafter paper I) are presented in §3, four cases are compared in §4, and in §5 we summarize and discuss the new results.

2. Simulation Setup

The code used in this study is a modified version of the TRISTAN code, a relativistic electromagnetic particle (REMP) code (Buneman 1993). Descriptions of PIC codes are presented in Dawson (1983), Birdsall & Langdon (1995), and Hickory & Eastwood (1988). This code has been used previously for many applications including astrophysical plasmas (Zhao et al. 1994; Nishikawa et al. 1997a).

Three simulations were performed using an $85 \times 85 \times 160$ grid with a total of 55 to 85 million particles (27 particles/cell/species for the ambient plasma) and an electron skin

depth, $\lambda_{ce} = c/\omega_{pe} = 4.8\Delta$, where $\omega_{pe} = (4\pi e^2 n_e/m_e)^{1/2}$ is the electron plasma frequency and Δ is the grid size. One simulation was performed using an $85 \times 85 \times 320$ grid with a total of 180 million particles (27 particles/cell/species for the ambient plasma) and an electron skin depth, $\lambda_{ce} = c/\omega_{pe} = 9.6\Delta$. In all simulations jets are injected at $z = 25\Delta$ in the positive z direction. In all simulations radiating boundary conditions were used on the planes at $z = 0, z_{max}$. Periodic boundary conditions were used on all other boundaries (Buneman 1993). The ambient and jet electron-positron plasma has mass ratio $m_e/m_p \equiv m_{e^-}/m_{e^+} = 1$. The electron thermal velocity in the ambient plasma is $v_{th} = 0.1c$ where c is the speed of light.

As in paper I, two kinds of jets have been simulated: a “thin” jet with radius $r_{jet} = 4\Delta$ and a “flat” (thick) jet that fills the computational domain in the transverse directions (infinite width). The thin jet is injected into a magnetized ambient plasma with magnetic field parallel to the jet. In two flat jet simulations, one is injected into an ambient plasma magnetized like the thin jet and one is injected into an unmagnetized ambient plasma. In one additional flat jet simulation on the longer grid a jet is injected into an unmagnetized ambient plasma but with half the plasma frequency and twice the skin depth so that $\lambda_{ce} = c/\omega_{pe} = 9.6\Delta$. The choice of parameters and simulations allows comparison with previous simulations (Silva et al. 2003; Frederiksen et al. 2003, 2004; Nishikawa et al. 2003), and also provides an investigation of skin depth, growth rate, and potential grid resolution effects.

3. Simulation results

3.1. Thin Jet Injection into Magnetized Ambient Plasma

The electron number density of the thin jet is $2.98n_b$, where n_b is the density of ambient (background) electrons. The average jet velocity $v_j = 0.9798c$, and the Lorentz factor is 5. The jet has thermal velocity $v_{j,th} = 0.01c$. The time step $t = 0.013/\omega_{pe}$, the ratio $\omega_{pe}/\Omega_e = 2.89$, and the Alfvén speed (for electrons) $v_{Ae} \equiv (\Omega_e/\omega_{pe})c = 0.346c$. Here $\Omega_e = eB/\gamma m_e$ is the electron cyclotron frequency. With the speed of an Alfvén wave given by $v_A = [V_A^2/(1+V_A^2/c^2)]^{1/2}$ where $V_A \equiv [B^2/4\pi(n_e m_e + n_p m_p)]^{1/2} = 0.245c$, the Alfvén Mach number $M_A \equiv v_j/v_A = 4.123$. With a magnetosonic speed $v_{ms} \equiv (v_{th}^2 + v_A^2)^{1/2}$ the Magnetosonic Mach number $M_{ms} \equiv v_j/v_{ms} = 3.795$. At least approximately the appropriate relativistic Mach numbers multiply these values by the Lorentz factor. Thus, in an MHD approximation we are dealing with a high Mach number shock with $\gamma M \gg 1$. The gyroradius of ambient electrons and positrons with $v_\perp = v_{th} = 0.1c$ is $1.389\Delta = 0.289\lambda_{ce}$. All the basic parameters are the same as in paper I except for the Alfvén wave speed in the ambient, $v_A \sim 0.075c$, which was reduced by the ion mass, $m_p = 20m_e$.

Figure 1 shows the jet electrons at simulation time $t = 22.1/\omega_{pe}$. The jet electrons are bunched along the jet direction and expanded transversely due to a two-stream-type instability. In this simulation the thin jet remains axisymmetric and behaves quite differently from the twisted thin electron-ion jet simulated in paper I. Since the radius of the thin jet is of the order of the electron skin depth and underresolved, it is not clear if the Weibel instability is excited. Nevertheless, the electron bunching seen in this case as opposed to the electron twisting seen in the electron-ion case illustrates the potential effect of ion mass on the two-stream instabilities. The differences between the two thin jet cases suggest excitation of the electrostatic two stream instability for the electron-positron jet and ambient medium as opposed to the Buneman electron-ion drift instability for the case of electron-ion jet and ambient medium. Since the diameter of the jet is too small compared to the skin depth and to realistic jets, further study will be performed using flat jets that fill the grid in the transverse direction.

3.2. Flat Jet Injection into Magnetized Ambient Plasma

The electron number density of the flat jet is $0.741n_b$. Ambient parameters are the same as in the case of the thin jet. In this case, the jet makes contact with the ambient plasma at a 2D interface spanning the computational domain. Here only the dynamics of the propagating jet head and shock region is studied. Effectively we study a small uniform portion of a much larger shock. This simulation system is different from simulations performed using counter-streaming equal number density particles spanning the computational domain in the transverse direction. The important differences between this type of simulation and previous counter-streaming simulations is that the evolution of the Weibel instability is examined in a more realistic spatial way including the motion of the jet head, and we can have different number densities in beam and ambient medium.

Electron density and current filaments resulting from development of the Weibel instability behind the jet front are shown in Figure 2 at time $t = 23.4/\omega_{pe}$. The electrons are deflected by the transverse magnetic fields (B_x, B_y) via the Lorentz force: $-e(\mathbf{v} \times \mathbf{B})$, generated by current filaments (J_z), which in turn enhance the transverse magnetic fields (Weibel 1959; Medvedev and Loeb 1999). The complicated filamented structures resulting from the Weibel instability have diameters on the order of the electron skin depth ($\lambda_{ce} = 4.8\Delta$). This is in good agreement with the prediction of $\lambda \approx 2^{1/4}c\gamma_{th}^{1/2}/\omega_{pe} \approx 1.188\lambda_{ce} = 5.7\Delta$ (Medvedev & Loeb 1999). Here, $\gamma_{th} \sim 1$ is a thermal Lorentz factor. The filaments are elongated along the direction of the jet (the z -direction, horizontal in Figure 2). The magnetic field and transverse current (J_x) shows significantly more transverse variation than was seen for the comparable electron-ion jet (Figure 2 in paper I).

The acceleration of electrons has been reported in previous work (Silva et al. 2003; Frederiksen et al. 2003, 2004; Nishikawa et al. 2003; Hedden et al. 2004) and is shown here in Figure 3. We see that the kinetic energy (parallel velocity $v_{\parallel} \approx v_j$) of the jet electrons is transferred to the perpendicular velocity via the electric and magnetic fields generated by the Weibel instability. The strongest transverse acceleration of jet electrons (Fig. 3a) accompanies the strongest deceleration of electron flow (Fig. 3b) and occurs between $z/\Delta = 100 - 120$. The transverse acceleration seen here is over four times that seen in the comparable electron-ion simulation in paper I at comparable simulation time (see Fig. 3 paper I) and the deceleration is also much greater. The strongest acceleration and deceleration takes place around the maximum amplitude of perturbations due to the Weibel instability at $z/\Delta \sim 105$ revealed qualitatively in Figure 2 and more quantitatively in Figure 4. Since the electrons and positrons have the same mass, they are accelerated equally perpendicular to the ambient magnetic field. At the jet front some jet electrons and positrons are accelerated and some are decelerated. This acceleration and deceleration is indicated by the slanting of the parallel velocity distribution at the jet head (Fig. 3b at $z = 136\Delta$). Furthermore, slight acceleration is found just behind the jet front ($z/\Delta \sim 130$). The positrons also have similar distributions (not shown). However, in paper I for the electron-ion case, only electrons have similar distributions as shown in Fig. 3b as ions have not had time to react. This fact is consistent with the electric field generated just behind the jet front. This may indicate that some Fermi acceleration is taking place at the jet front as described in previous work (e.g., Achterberg et al. 2001; Gallant 2002; Ellison & Double 2002), however, further investigation is necessary. Figure 3 suggests that the “acceleration region” has a thickness in the range $z/\Delta = 70 - 130$ behind the front defined by the fastest moving jet electrons. Possibly, the “turbulence” assumed for the diffusive shock acceleration (DSA) corresponds to this shock region (downstream but not upstream).

The ambient electrons and positrons are also accelerated, e.g., Fig. 3c & 3d. Some of the ambient electrons are accelerated perpendicularly up to $0.6c$ and are accelerated in the direction of jet flow to greater than $0.6c$. The leading edge as defined by the fastest jet electrons is not significantly reduced as would be the case for the jet head in an ideal relativistic MHD simulation (e.g., Nishikawa et al. 1997b). An ideal MHD simulation would give a head advance speed

$$v_h \sim \frac{\gamma\eta^{1/2}}{1 + \gamma\eta^{1/2}} v_j = 0.81c ,$$

where $\eta = n_j/n_b = 0.741$ and we have ignored magnetic and thermal pressures in the ram pressure balance equation (Martí et al. 1997; Rosen et al. 1999). On the other hand, the average forward motion of the most decelerated jet particles and most accelerated ambient particles is of this order.

Figure 4 shows 1-D cuts through the computational grid parallel to the z -axis at $x/\Delta = 38$ and three locations $y/\Delta = 38, 43$, and 48 separated approximately by the electron skin depth ($\lambda_{ce} \sim 4.8\Delta$). This figure provides some quantitative longitudinal information about the filament structures shown qualitatively in Figure 2. With separation by about a skin depth the phase of the instability is different along different cuts, but the amplitudes are similar. The growth time of the Weibel instability is calculated to be, $\tau \approx \gamma_{sh}^{1/2}/\omega_{pe}$ (Medvedev & Loeb 1999) and here $\tau \approx 2.2/\omega_{pe}$ with $\gamma_{sh} = 5$. If this is converted into a growth length $\ell \equiv c\tau = 2.2\lambda_{ce} \sim 10.7\Delta$. The simulation results show that the maximum amplitudes are achieved at $z \sim 105\Delta$ about 80Δ from the position of the jet injection at $z = 25\Delta$. This result indicates that the Weibel instability grows to maximum amplitude from thermal fluctuations in about eight growth lengths (eight growth times) at $t = 23.4/\omega_{pe}$. The electron density shown in Fig. 4a indicates that the width of the jet head is slightly larger than the electron skin depth, 4.8Δ . A similar feature is not obvious in the electron-ion case (see Fig. 4a in paper I). The fluctuation amplitudes in the nonlinear stage for the electron-positron case shown here in Figure 4 are much larger than in the electron-ion case considered in paper I at the same time (see Fig. 4 in paper I). The electron density fluctuates by nearly a factor 2 about the average, whereas in the electron-ion case the fluctuation was by less than a factor 1.2 about the average.

The z -component of current density shown in Fig. 4b indicates both positive and negative currents in the jet head region and shows no evidence for the small negative current found at the leading edge of the electron-ion jet in paper I. In the electron-ion “shock” some jet electrons are ahead of the ions. Fluctuations in this component of the current density are up to a factor 3 times larger than in the electron-ion case. Here the electric field amplitude is up to 4 times greater than that found in the electron-ion case. The induced transverse magnetic fields are up to 10 times those found in the electron-ion case. Based on Figs. 2 and 4 the length of filaments along the jet, $\sim 10\Delta$, around $z = 100\Delta$ is approximately twice the electron skin depth. This result is consistent with the previous electron-positron simulations performed by Silva et al. (2003).

Transverse structure accompanying the Weibel instability is shown by 2-D slices of the longitudinal current density and electron density along with the transverse magnetic field in Figure 5. The size of these structures transverse to the jet propagation is about the electron skin depth. Such transverse structures are also found in counter-streaming jet simulations (Silva et al. 2003; Frederiksen et al. 2003, 2004). The simulation results also show that smaller scale filaments have merged into larger scale filaments in the nonlinear stage at the maximum amplitudes (see also Silva et al. 2003; Frederiksen et al. 2004; Medvedev et al. 2004).

3.3. Unmagnetized Ambient Plasma and Electron Skin Depth

The simulations of Silva et al. (2003) and Frederiksen et al. (2003, 2004) did not include ambient magnetic fields. We have performed one flat jet simulation without ambient magnetic fields but otherwise identical to the flat electron-positron jet injection into a magnetized electron-positron plasma. Here we can compare results with these previous simulations, with our electron-ion jet injection into an unmagnetized electron-ion plasma in paper I and evaluate the effect of ambient magnetic fields on the perturbations. Additionally, we have performed one flat jet simulation using a different electron skin depth, $\lambda_{ce} = c/\omega_{pe} = 9.6\Delta$. Here the electron plasma frequency is half of that used in the original simulations, and the system size is two times longer than the original size. This allows us to evaluate the effect of the electron skin depth on the size of structures, the dependence of growth rate on the plasma frequency, and the potential effect of our grid scale on the results.

The filamentary structure of electron density, magnetic fields and currents resulting from development of the Weibel instability is shown in Figure 6a & 6b for $\lambda_{ce} = 4.8\Delta$ and in Figure 6c & 6d for $\lambda_{ce} = 9.6\Delta$. Comparison between Figs. 6a & 6b and Figure 2 reveals little qualitative change in density, current or magnetic structure resulting from an ambient magnetic field. Quantitatively, the peak values of the perturbations due to the Weibel instability for an unmagnetized ambient plasma are somewhat larger, 20 - 25%, than those for a magnetized ambient plasma. Comparison of Figs. 6a & 6b with Figs. 6c & 6d shows that a doubling of the electron skin depth has resulted in a predicted doubling of the size of structures, both transversely and longitudinally. Filamentary structures appear about twice as far behind the leading edge defined by the fastest moving jet particles. This doubling of structure size is the expected result if structures scale with the electron skin depth (Medvedev & Loeb 1999). The fact that we find this scaling indicates sufficient grid resolution when $\lambda_{ce} = 4.8\Delta$ and with $\lambda_{Debye} \sim 0.5\Delta$.

Transverse structure in the electron and current density, and in the transverse magnetic field for the two different electron skin depths is shown in a 2-D slice in the $x - y$ plane at $t = 23.4/\omega_{pe}$ in Figure 7. Figures 7a and 7b correspond to Figs. 5a and 5b, which show that the weak initial ambient magnetic field does not affect on the evolution of Weibel instability. The grid size is the same for all panels, it is easy to see that the structures with twice the electron skin depth are approximately two times larger. The increase in size makes it easy to see (Fig. 7d) that the transverse magnetic field ($B_{x,y}$) is toroidal around the current filaments (J_z) represented by the color contours. In internal shocks, typical plasma densities of $n_e \sim 3 \times 10^{10} \text{ cm}^{-3}$, shock Lorentz factors $\gamma_{sh} \sim 4$ and initial thermal Lorentz factors, $\gamma_{th} \sim 2$, yield plasma frequencies $\omega_e \sim 1 \times 10^9$, and electron skin depth $\sim 50 \text{ cm}$ (eq. 9a in Medvedev & Loeb (1999)). At least approximately this gives an indication as to our filament

size in the shock reference frame in a GRB. This scale is much smaller than any observed spatial scale associated with the source. In an external shock $n_e \approx 4.3\text{cm}^{-3}$, $\gamma_{\text{sh}} \approx 39$, the relativistic electron skin depth ($= c\gamma_{\text{sh}}^{1/2}/\omega_e$) is $\sim 10^6$ cm (Frail et al. 2004).

The longitudinal structure of perturbations along the z -direction in J_z , and B_x for the two different skin depths is shown in Figure 8. Here the 1-D cuts through the computational grid parallel to the z -axis are located at $y/\Delta = 38, 43$, and 48 ($\lambda_{\text{ce}} = 4.8\Delta$) or $y/\Delta = 33, 43$, and 53 ($\lambda_{\text{ce}} = 9.6\Delta$) and are separated approximately by an electron skin depth. Here we see that the lengths of filamentary structures are doubled by the doubled skin depth as expected. The only obvious difference is a reduction in the maximum transverse magnetic field by almost a factor of two. Note also some accompanying reduction in the typical current density, J_z . Since current density maxima are comparable for both skin depths it seems likely that differences here are largely an accidental result of the location of the cuts. Note how similar the results seen in Figs. 8a and 8b are to those shown in Figs. 4b & 4c with an initial ambient magnetic field. The modest differences are a result of the different seed perturbations (thermal noise caused by the initial loading of particles).

4. Electron-Positron, Electron-Ion Results Compared

The efficiencies of conversion of bulk kinetic energy into radiation via synchrotron or “jitter” emission from relativistic shocks will be determined by the magnetic field strength and the electron energy distribution behind the shock. In what follows we examine the conversion of bulk kinetic energy into magnetic and thermal energy by comparing the relevant energy densities in a volume consisting of a number of cells. The simulations show that the initial jet bulk kinetic energy is converted into magnetic energy, transverse acceleration of the jet and ambient particles (thermal energy), and acceleration of the ambient plasma through the Weibel instability.

In order to compare characteristics of Weibel instabilities, we have evaluated the magnetic field energy, ambient electron thermal energy and jet electron thermal energy for four different cases at $t = 23.4/\omega_{\text{pe}}$, all without initial ambient magnetic fields. For the electron-positron jet and ambient we calculated these quantities for the two different skin depths (case A (smaller skin depth) and case B (larger skin depth)) considered in this paper as shown in Figures 6, 7, and 8. The values obtained here are compared to similar values obtained for electron-ion jet and ambient considered in paper I (case C) shown in Figures 7, 8, and 9 in paper I. Additionally, we have performed a new electron-ion simulation with a larger skin depth (case D) that can be compared to case B in this paper. The volumes over which averages are determined include all cells to the transverse boundaries of the grid between limiting z distances. For the larger skin depth (cases B and D) shocked quantities

are calculated in the region $155 < z/\Delta < 215$ where the Weibel instability has largest amplitudes, and ambient quantities are calculated in the injection region $25 < z/\Delta < 85$ where the Weibel instability has not been excited. For cases A and C with the smaller skin depth, shocked quantities are calculated in the region $90 < z/\Delta < 120$ and ambient quantities are obtained in the region $25 < z/\Delta < 55$.

The thermal energy contained in the chosen volume is given by $U_{\text{th}} = \sum(\gamma_{\text{th}} - 1)m_n c^2$ where $\gamma_{\text{th}} = [1 - (v_{\text{th}}/c)^2]^{-1/2}$ and where the summation is over the number of particles, m_n is the mass of particle n , and $v_{\text{th}} = [(v_{\parallel}^{\text{th}})^2 + (v_{\perp}^{\text{th}})^2]^{1/2}$, is the thermal velocity for particle n . Here we define the components of the individual particle's velocity parallel to the bulk velocity, $v_{\parallel} \equiv (\mathbf{v} \cdot \mathbf{V})/V$, and perpendicular to the bulk velocity, $v_{\perp} \equiv |\mathbf{v} \times \mathbf{V}|/V$, where \mathbf{v} and \mathbf{V} represent the motion of particle n and the bulk motion of particles, respectively ($V = [V_x^2 + V_y^2 + V_z^2]^{1/2}$). We define the velocity of the bulk motion $\mathbf{V} = \sum \mathbf{v}/n_{\text{cell}}$, where we sum the velocities, \mathbf{v} , over n_{cell} number of particles in the grid zone. The parallel and perpendicular components of the thermal velocity are given by

$$v_{\parallel}^{\text{th}} = \frac{v_{\parallel} - V}{1 - \mathbf{v} \cdot \mathbf{V}/c^2},$$

and

$$v_{\perp}^{\text{th}} = \frac{v_{\perp}}{\Gamma_V(1 - \mathbf{v} \cdot \mathbf{V}/c^2)},$$

where $\Gamma_V = [1 - (V/c)^2]^{-1/2}$. In general, we must separately compute bulk and thermal energy for each particle species as bulk motion and thermal velocity can be different for each species, here electrons, e , positrons, p , and ions, i . For our purposes it can also be useful to separate the ambient, a , particles from the jet, j , particles and to compare initial, in , and shocked, sh , states. For example, $U_B^{\text{sh}} = B_{\text{sh}}^2/8\pi$, represents the shocked value of the magnetic energy, and $U_{\text{th}}^{\text{e},j,\text{sh}} = \sum(\gamma_{\text{th}} - 1)m_e c^2$, where $\gamma_{\text{th}} = [1 - (v_{\text{th}}^{\text{e},j,\text{sh}}/c)^2]^{-1/2}$ and $U_V^{\text{e},j,\text{sh}} = \sum(\Gamma_V - 1)m_e c^2$, where $\Gamma_V = [1 - (V^{\text{e},j,\text{sh}}/c)^2]^{-1/2}$, represent the shocked values of the jet electron thermal energy, and jet electron bulk kinetic energy, respectively. The total kinetic energy is written $U_k^{\text{e},j,\text{sh}} = \sum(\gamma_k - 1)m_e c^2$, where $\gamma_k = [1 - (v^{\text{e},j,\text{sh}}/c)^2]^{-1/2}$.

At the comparable simulation time perturbations associated with the Weibel instability grow to a larger amplitude for the electron-positron jet and ambient than for the comparable electron-ion case. A comparison between the magnetic field energy, U_B^{sh} , in the shock region (all values in simulation units) for electron-positron, and electron-ion cases shows: (A) $U_B^{\text{sh}} = 4.484 \times 10^4$, (B) $U_B^{\text{sh}} = 4.088 \times 10^4$, (C) $U_B^{\text{sh}} = 2.884 \times 10^3$, and (D) $U_B^{\text{sh}} = 1.824 \times 10^3$. The values in the cases A and C are multiplied by two since the volume over which these numbers are obtained is half of that used for cases B and D. This comparison reveals that the magnetic energy growth accompanying growth of the Weibel instability is about 20 times larger for electron-positron jet and ambient than for the comparable electron-ion cases.

The increase in magnetic field energy above the initial thermal fluctuations is calculated to be: (A) $U_B^{\text{sh}}/U_B^{\text{in}} = 4.860 \times 10^3$, (B) $U_B^{\text{sh}}/U_B^{\text{in}} = 6.080 \times 10^3$, (C) $U_B^{\text{sh}}/U_B^{\text{in}} = 1.646 \times 10^3$, and (D) $U_B^{\text{sh}}/U_B^{\text{in}} = 1.140 \times 10^3$. These values show that the magnetic field energy for electron-positron jet and ambient plasma is increased about four times more than for the comparable electron-ion ($m_i/m_e = 20$) jet and ambient plasma.

The increase in thermal energy of the jet electrons for the four cases is calculated using the above definitions to be: (A) $U_{\text{th}}^{\text{e,j,sh}}/U_{\text{th}}^{\text{e,j,in}} = 16.13$, (B) $U_{\text{th}}^{\text{e,j,sh}}/U_{\text{th}}^{\text{e,j,in}} = 12.81$, (C) $U_{\text{th}}^{\text{e,j,sh}}/U_{\text{th}}^{\text{e,j,in}} = 1.73$, and (D) $U_{\text{th}}^{\text{e,j,sh}}/U_{\text{th}}^{\text{e,j,in}} = 1.31$. The thermal energy of jet electrons in the electron-positron jet is increased about ten times more than in the comparable electron-ion jet.

If we compare the magnetic field energy in the shocked region to the initial total kinetic energy, i.e., $\epsilon_B^k = U_B^{\text{sh}}/(U_k^{\text{j,in}} + U_k^{\text{a,in}})$, we find: (A) $\epsilon_B^k = 1.01 \times 10^{-2}$, (B) $\epsilon_B^k = 1.02 \times 10^{-2}$, (C) $\epsilon_B^k = 0.72 \times 10^{-4}$, and (D) $\epsilon_B^k = 0.45 \times 10^{-4}$. For the electron-ion jet and ambient plasma $\epsilon_B^k \approx 10^{-4}$ in agreement with the linear theory predictions made by Wiersma & Achterberg (2004). However, it should be noted that in our electron-ion simulations the mass ratio $m_i/m_e = 20$ and nonlinear saturation has not been fully achieved and this may explain the agreement with a linear prediction. In any event, for the electron-positron jet and ambient plasma $\epsilon_B^k \approx 10^{-2}$, which may be in the nonlinear phase and is at least two orders of magnitude larger. This result is consistent with the efficiencies required by the observed synchrotron radiation (Gruzinov & Waxman 1999).

For the case B the average jet electron velocity (V_z) in the shock region ($155 < z/\Delta < 215$) is reduced to $V_z = 0.9656c$ from an initial $V_z = 0.9765c$ ($25 < z/\Delta < 85$). This result indicates the slow down accompanying excitation of the Weibel instability. Calculation of the decrease in jet electron bulk kinetic energy, $\epsilon_V \equiv U_V^{\text{e,j,sh}}/U_V^{\text{e,j,in}}$, for the four cases reveals: (A) $\epsilon_V = 0.737$, (B) $\epsilon_V = 0.805$, (C) $\epsilon_V = 0.976$, and (D) $\epsilon_V = 0.990$. We see at least a 20 - 25% conversion of bulk kinetic jet energy into magnetic fields, thermalization of jet and ambient plasma, and acceleration of ambient plasma for an electron-positron jet and ambient. The maximum efficiency for the electron-ion jet at this simulation time is 1 - 3%. During these simulation times ions do not slow down with the electrons and the efficiency is reduced by a factor up to $m_e/m_i = 20$ as the total initial bulk kinetic energy of electrons and ions is about 20 times larger. In order to fully take account of ion involvement in the Weibel instability, simulations with a longer system and a longer simulation time are required ($(m_i/m_e)^{1/2} \sim 4 - 5$) (Frederiksen et al. 2004; Hedeland et al. 2004).

Calculation of the increase in thermal energy of ambient electrons for the four cases shows that: (A) $U_{\text{th}}^{\text{e,a,sh}}/U_{\text{th}}^{\text{e,a,in}} = 8.38$, (B) $U_{\text{th}}^{\text{e,a,sh}}/U_{\text{th}}^{\text{e,a,in}} = 8.47$, (C) $U_{\text{th}}^{\text{e,a,sh}}/U_{\text{th}}^{\text{e,a,in}} = 1.32$, and (D) $U_{\text{th}}^{\text{e,a,sh}}/U_{\text{th}}^{\text{e,a,in}} = 1.22$. In the electron-positron ambient plasma, the thermal energy

of electrons and positrons is increased about 6 times more than thermal energy of the electrons in the electron-ion ambient plasma. The electron-positron shock is much quicker at converting bulk kinetic energy into thermal energy (particle acceleration) and magnetic field energy.

5. Summary and Discussion

We have performed self-consistent, three-dimensional relativistic particle simulations of relativistic electron-positron jets propagating into magnetized and unmagnetized electron-positron ambient plasmas. The main acceleration of electrons takes place in the downstream region. Processes in the relativistic collisionless shock are dominated by structures produced by the Weibel instability. This instability is excited in the downstream region behind the jet head, where electron density perturbations lead to the formation of current filaments. The nonuniform electric field and magnetic field structures associated with these current filaments decelerate the jet electrons and positrons, while accelerating the ambient electrons and positrons, and accelerating (heating) the jet and ambient electrons and positrons in the transverse direction.

Two new findings are confirmed in this study. As shown in the previous sections, density, current, electric and magnetic field amplitudes for electron-positron jet and plasma are significantly larger than the those for a comparable electron-ion jet and plasma at similar simulation time. In the electron-positron plasma, both electron and positrons participate in exciting the Weibel instability. Transverse acceleration and deceleration of the jet particles, an acceleration of the ambient particles, and transverse acceleration (heating) of jet and ambient particles inside the “shock” region is significantly larger than in the electron-ion case as described in the previous sections. However, we evaluate our electron-ion results at the similar simulation time to our electron-positron results. At this simulation time ions have not yet participated in the dynamics significantly. At long time and longer spatial scales, the ion dynamics becomes dominant (e.g., Hededal et al. 2004).

Secondly, comparison between simulations with different plasma frequency reveals the expected growth rate decrease as the plasma frequency decreases. This is accompanied by the expected growth length and filament size increase as the electron skin depth, $\lambda_{ce} \propto \omega_{pe}^{-1}$, increases as shown in Figs. 6, 7, and 8.

The Weibel instability originates from the fact that the electrons are deflected by the perturbed (small) transverse magnetic fields accompanying the current filaments and subsequently enhance the current filaments (Weibel 1959; Medvedev & Loeb 1999; Brainerd 2000; Gruzinov 2001). The deflection of particles due to the Lorentz force increases as the

magnetic field perturbation grows in amplitude. Our results here are consistent with results from previous simulations (Silva et al. 2003; Frederiksen et al. 2003, 2004).

The basic nature of the Weibel instability (Medvedev & Loeb 1999; Nishikawa et al. 2003) is also confirmed in this study of electron-positron jet cases. In particular, the aperiodic nature of the instability ($\omega_{\text{real}} = 0$ (convective)) is observed in the evolution of the generated transverse magnetic field (B_y). Thus, it can be saturated only by nonlinear effects and not by kinetic effects, such as collisionless damping or resonance broadening. Hence the magnetic field can be amplified to very high values locally as shown in Figs. 7b and 7d..

In general, we find that the absence of an ambient magnetic field leads to slightly larger maximum values for the perturbations produced by the Weibel instability. Qualitatively there appears to be little change in the current filament and transverse magnetic field structure resulting from the ambient magnetic field that we have considered here. This result is similar to that found previously for the flat electron-ion jet injected into a magnetized and unmagnetized electron-ion plasma. Thus, our present ambient magnetic field oriented parallel to the flow direction with Alfvén wave speed greater than the thermal speed for the the electron-positron plasma or less than the thermal speed for the electron-ion plasma, has only a minor influence on the results.

The perturbed electron density and filamented currents have a complicated three-dimensional structure. The transverse size of these structures is on the order of the electron skin depth and is somewhat larger if there are no ambient magnetic fields. However, the length of structures along the jet direction is slightly larger than the transverse scale. At the termination of our simulations, for an electron skin depth $\lambda_{\text{ce}} = 4.8\Delta$ the thickness of the unstable region along the jet direction ranges from $z/\Delta = 55$ to 135 , is $\gtrsim 15\lambda_{\text{ce}}$, and is similar for electron-ion jets and plasma.

The perturbation size in the transverse direction become largest around $z/\Delta = 105$ where nonlinear effects lead to the merging of the smaller scale filaments that first appear behind the jet front. This result is similar to previous counter-streaming simulations (Silva et al. 2003; Frederiksen et al. 2004; Medvedev et al. 2004) in which smaller filaments first appear and then merge into larger filaments at a later time. Now we see the temporal development appear as a spatial development and this occurs about eight growth lengths, $8\ell \sim 6.5c/\omega_{\text{pe}} \sim 80\Delta$ from the position of the jet injection.

Recent observations show that from optical observations alone the wiggles in the light curves of GRB 011211 are the result of spherically asymmetric density or energy variations, i.e. variations that cover less than the observed $1/\gamma$ region (Jakobsson et al. 2004). The $1/\gamma$ region has a transverse size of $\sim r/\gamma$ where r is the radial distance to the gamma-ray

emitting region. With $10^{14} \leq r \leq 10^{16}$ cm the variations need only be somewhat smaller than say 10^{12} cm. Collisionless shocks mediated by the Weibel instability have density and current structures with sizes on the order of the electron skin depth. The typical transverse Weibel filament size $\lambda_{ce} \sim \gamma^{1/2}c/\omega_{pe} \sim 3 \times 10^{11}/\omega_{pe}$, where here the relevant value of the plasma frequency in the observer’s frame for the Weibel instability is $\omega_{pe}/\gamma^{1/2}$. We note that the length of filaments will be subject to length contraction but since the longitudinal plasma frequency is $\omega_{pe}/\gamma^{3/2}$ the filament aspect ratio should be preserved. The resultant size for any reasonable estimate of the plasma frequency is many orders of magnitude smaller than the asymmetric density variations implied by the light curves. Thus, the gamma-ray burst may be composed of emission from many different regions but with variation from region to region on much larger scales than those we have considered here. Since we found little difference between no magnetic field and modest magnetic field (the Alfvén wave speed was on the order of the thermal speed), we might expect our present results to apply in the presence of magnetic fields with magnetic energy in equipartition with the thermal energy in the downstream region.

The generation of magnetic fields both with and without an initial magnetic field suggests that emission in GRB afterglows and Crab-like pulsar winds could be either synchrotron or jitter emission (Medvedev 2000). The size of filaments appear to be smaller than can produce observable variations in intensity structure. However, this small size can mean that the deflection angle, $\alpha \sim eB_{\perp}\lambda_B/\gamma m_e c^2$, of particles by Weibel filaments is smaller than the radiation beaming angle, $\Delta\theta \sim 1/\gamma$ (Medvedev 2000). Here $\lambda_B \sim \lambda_{ce}$, $eB_{\perp}/m_e c < \Omega_e$, and the ratio $\delta \sim \alpha/\Delta\theta < \Omega_e/\omega_{pe}$ will be less than one when the cyclotron frequency is less than the plasma frequency. Thus, when ambient magnetic fields are moderate, i.e., the cyclotron frequency is less than the plasma frequency and $\delta < 1$, the emission may correspond to jitter rather than synchrotron radiation.

Our simulation studies have provided a framework for the dynamics of a relativistic shock generated within an electron-positron or an electron-ion relativistic jet. The Lorentz factor $\gamma = 5$ set of simulations is appropriate to internal shocks resulting from faster material overtaking slower material in the reference frame of the slower material, ambient medium in our simulations. Here the “shock” Lorentz factor, γ_{sh} , can be related most simply to the Lorentz factors of high, γ_h , and low, γ_{ℓ} , speed material with

$$\gamma_{sh} = \epsilon\gamma_h^2[1 - (1 - 1/\gamma_h^2)^{1/2}(1 - 1/(\epsilon\gamma_h)^2)^{1/2}]$$

where $1 \geq \epsilon \equiv \gamma_{\ell}/\gamma_h \geq 1/\gamma_h$. Provided $\gamma_h \gg 10$, $\gamma_{sh} \sim 5$ implies $\epsilon \sim 1/10$. For example, our present simulation set is relevant to internal AGN jet shocks produced by $\gamma_h \sim 20$ material overtaking $\gamma_{\ell} \sim 2$ material and to internal GRB shocks produced by $\gamma_h \sim 300$ material overtaking $\gamma_{\ell} \sim 30$ material.

The fundamental characteristics of relativistic shocks are essential for a proper understanding of the prompt gamma-ray and afterglow emission in gamma-ray bursts, and also to an understanding of the particle reacceleration processes and emission from the shocked regions in relativistic AGN jets. Since the shock dynamics is complex and subtle, more comprehensive studies are required to better understand the acceleration of electrons, the generation of magnetic fields and the associated emission. This further study will provide the insight into basic relativistic collisionless shock characteristics needed to provide a firm physical basis for modeling the emission from shocks in relativistic flows.

K. Nishikawa is a NRC Senior Research Fellow at NASA Marshall Space Flight Center. The author K.I.N. thanks useful discussions with Christian Hededal. This research (K.N.) is partially supported by the National Science Foundation awards ATM 9730230, ATM-9870072, ATM-0100997, and INT-9981508. P. Hardee acknowledges partial support by a National Space Science & Technology (NSSTC/NASA) award. The simulations have been performed on ORIGIN 2000 and IBM p690 (Copper) at the National Center for Supercomputing Applications (NCSA) which is supported by the National Science Foundation.

REFERENCES

Achterberg, A., Gallant, Y.A., Kirk, J.G., & Guthmann, A.X. 2001, MNRAS, 328, 393

Birdsall, C.K., & Langdon, A.B., 1995, *Plasma Physics via Computer Simulation*, McGraw-Hill, second Edition

Brainerd, J.J. 2000, ApJ, 538, 628

Buneman, O., 1993, *Tristan*, in *Computer Space Plasma Physics: Simulation Techniques and Software*, edited by H. Matsumoto Matsumoto & Y. Omura, p. 67, Terra Scientific Publishing Company, Tokyo

Dawson, J.M. 1983, Rev. Mod. Phys., 55, 403

Ellison, D.C., & Double, G.P. 2002, Astroparticle Phys., 18, 213

Frail, D. A., Soderberg, A. M., Kulkarni, S. R., Berger, E., Yost, S., Fox, D. W., & Harrison, F. A. 2004, ApJ, submitted, (astro-ph/0408002)

Frederiksen, J.T., Hededal, C.B., Haugbølle, T., & Nordlund, Å. 2003, Proc. From 1st NBSI on Beams and Jets in Gamma Ray Bursts, held at NBIfAFG/NORDITA, Copenhagen, Denmark, August, 2002, (astro-ph/0303360)

Frederiksen, J.T., Hededal, C.B., Haugbølle, & Nordlund, Å. 2004, ApJ, 608, L13

Gallant, Y.A., 2002, Particle Acceleration at Relativistic Shocks, in Relativistic Flows in Astrophysics, eds. A.W. Guthmann, M. Georganopoulos, A. Marcowith, & K. Manolokou, Lecture Notes in Physics, Springer Verlag., (astro-ph/0201243)

Gruzinov, A. 2001, ApJ, 563, L15

Gruzinov, A. & Waxman, E. 1999, ApJ, 511, 852

Hededal, C.B., Haugbølle, Frederiksen, J.T., & Nordlund, Å. 2004, ApJ, submitted, (astro-ph/0408558)

Hickory, R.W., & Eastwood, J.W., 1988, Computer Simulation using Particles, McGraw-Hill, second edition

Jakobsson, P., Hjorth, J., Ramirez-Ruiz, E. 12 more, 2004, New Astron, 9, 435

Niemiec, J., & Ostrowski, M. 2004, ApJ, 610, 851

Martí, J.M., Müller, E., Font, J.A., Ibáñez, J.M., & Marquina, A. 1997, ApJ, 479, 151

Medvedev, M.V. 2000, ApJ, 540, 704

Medvedev, M.V. & Loeb, A. 1999, ApJ, 526, 697

Medvedev, M.V., Fiore, M., Fonseca, R. A., Silva, L. O., & Mori, W. B. 2004, ApJL, submitted (astro-ph/0409382)

Nishikawa, K.-I., Zhao, J., Sakai, J.I., & Neubert, T. 1997a, Adv. Space. Res., 19, (1)117

Nishikawa, K.-I., Koide, S., Sakai, J.-I., Christodoulou, D.M., Sol, H., & Mutel, R.L. 1997b, ApJ, 483, L45

Nishikawa, K.-I., Hardee, P., Richardson, G., Preece, R., Sol, H., & Fishman, G.J. 2003, ApJ, 595, 555

Ostrowski, M., & Bednarz, J. 2002, A&A, 394, 1141

Pruet, J., Abazajian, K., Fuller, G. M. 2001, Phys. Rev. D., 64, 063002-1

Rosen, A., Hughes, P.A., Duncan, G.C., & Hardee, P.E. 1999, ApJ, 516, 729

Rossi, E., & Rees, M.J. 2003, MNRAS, 339, 881

Schlickeiser, R., Vainio, R., Böttcher, M., Lerche, I., Pohl, M., & Schuster, C. 2002, A&A, 393, 69

Silva, L. O., Fonseca, R. A., Tonge, J., W., Dawson, J. M., Mori, W.B., & Medvedev, M. V., 2003, ApJ, 596, L121

Weibel, E.S. 1959, Phys. Rev. Lett., 2, 83

Wiersma, J. & Achterberg, A. 2004, A&A, submitted, (astro-ph/0408550)

Zhao, J., Sakai, J.I., Nishikawa, K.-I., & Neubert, T. 1994, Phys. Plasmas, 1, 4114

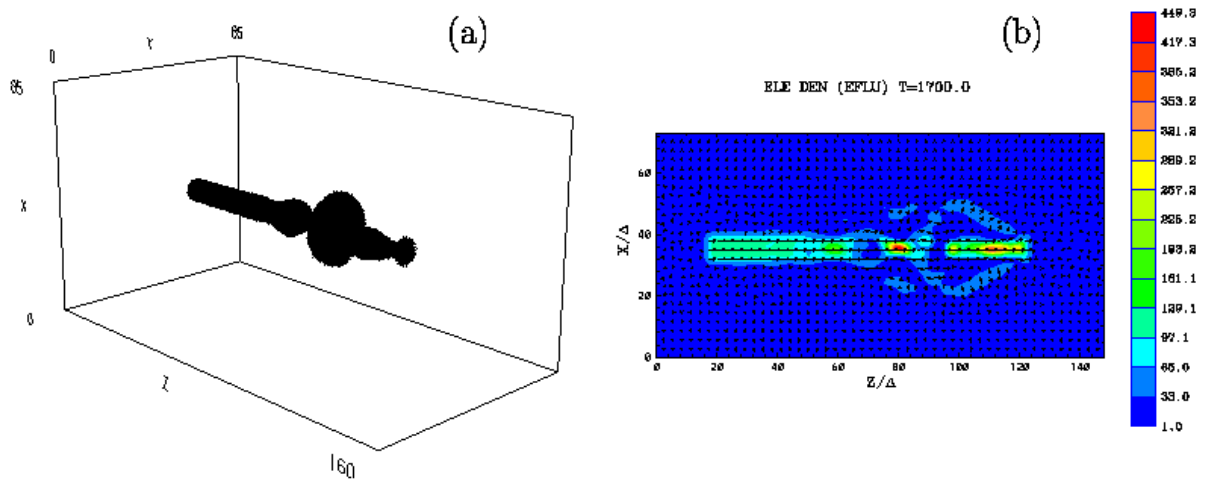


Fig. 1.— Dynamics of a thin jet are indicated at $t = 22.1/\omega_{pe}$ by (a) a jet electron image in the 3-dimensional simulation system, and (b) the total electron density in the $x - z$ plane in the center of the jet with the electron flux indicated by arrows and density indicated by color.

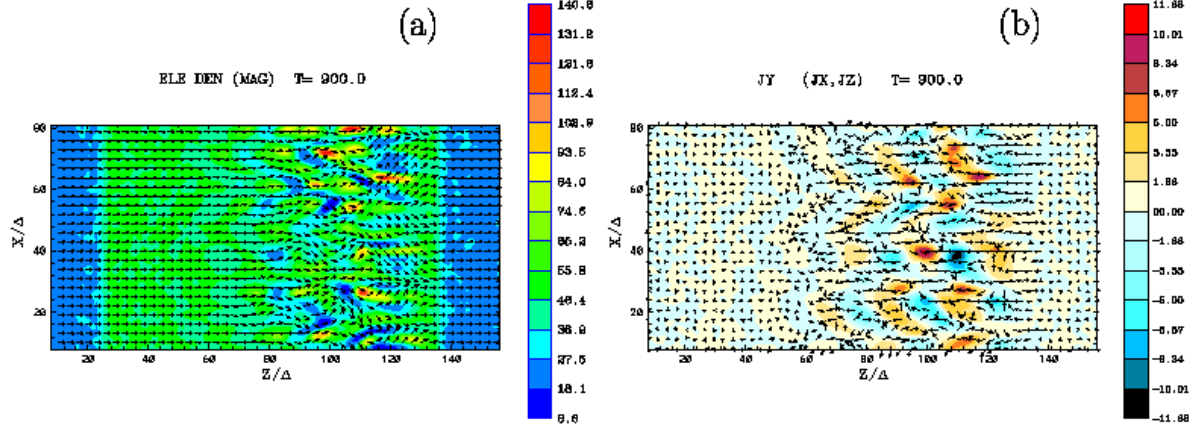


Fig. 2.— 2D images in the $x - z$ plane at $y = 43\Delta$ for a flat jet injected into a magnetized ambient medium shown at $t = 23.4/\omega_{pe}$. In (a) color indicates the electron density (peak: 140.6) with magnetic fields represented by arrows and in (b) color indicates the y -component of the current density (J_y) (peak: 11.8) with J_z, J_x indicated by the arrows.

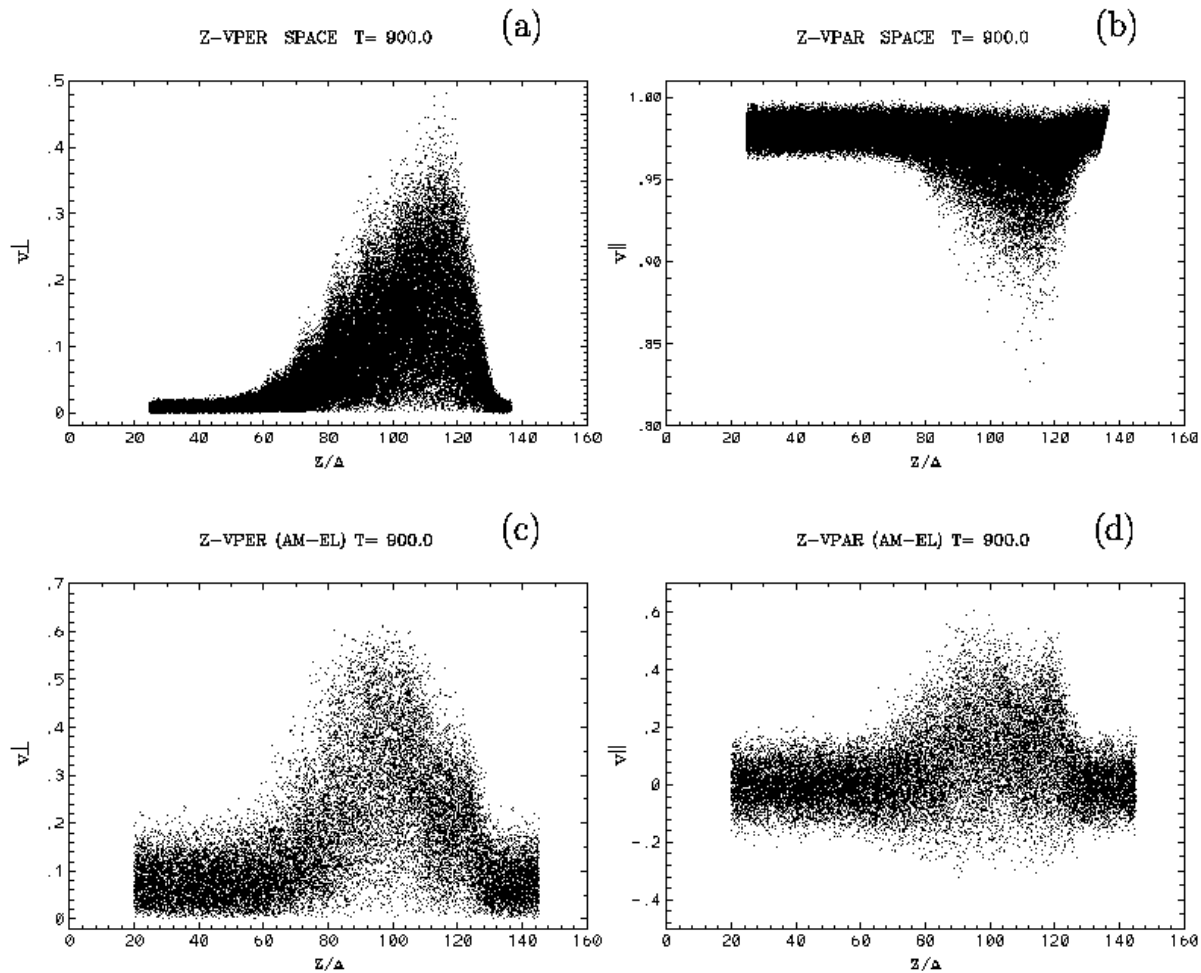


Fig. 3.— The distribution of jet and ambient electrons at $t = 23.4/\omega_{pe}$ in (a) $z - v_{\perp}/c$ (jet), (b) $z - v_{\parallel}/c$ (jet), (c) $z - v_{\perp}/c$ (ambient), (d) $z - v_{\parallel}/c$ (ambient) phase space. Roughly 20% of the jet electrons and 0.1% of the ambient electrons ($20 < z/\Delta < 145$) are randomly selected for these plots.

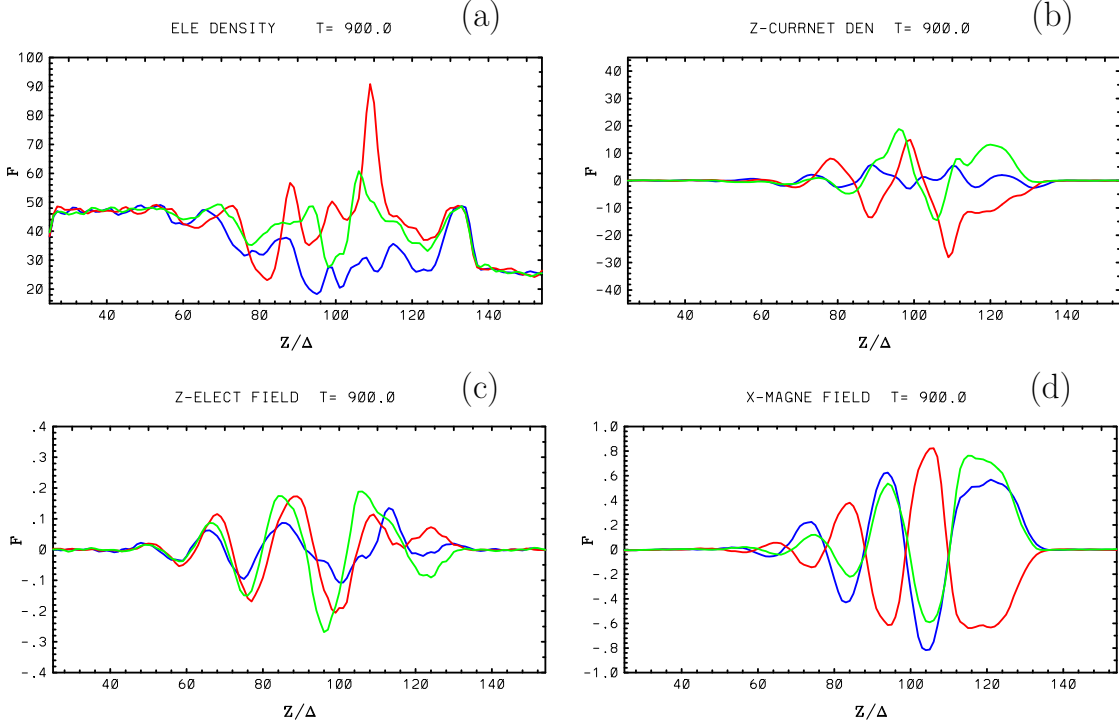


Fig. 4.— One-dimensional cuts along the z -direction ($25 \leq z/\Delta \leq 154$) of a flat jet. Shown are (a) the electron density, (b) the z -component of the current density, (c) the z -component of the electric field, and (d) the x -component of the magnetic field shown at $t = 23.4/\omega_{pe}$. Cuts are taken at $x/\Delta = 38$ and $y/\Delta = 38$ (blue-dotted), 43 (red-solid), 48 (green-dashed) and separated by about one electron skin depth.

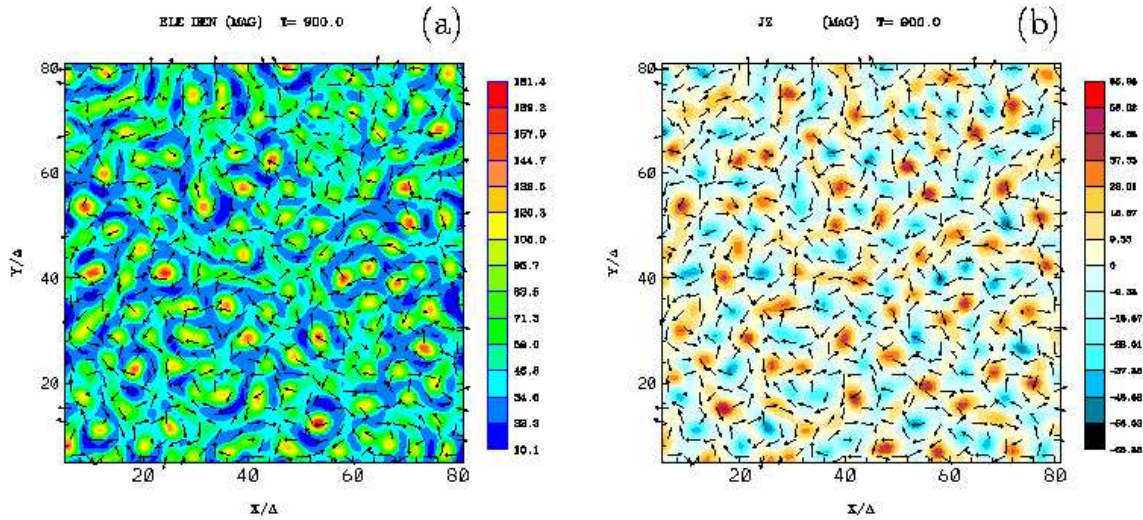


Fig. 5.— The electron density (a) and z-component of the current density (b) in the $x - y$ plane is plotted at $z/\Delta = 120$ at $t = 23.4/\omega_{pe}$. The arrows show the transverse magnetic fields $B_{x, y}$.

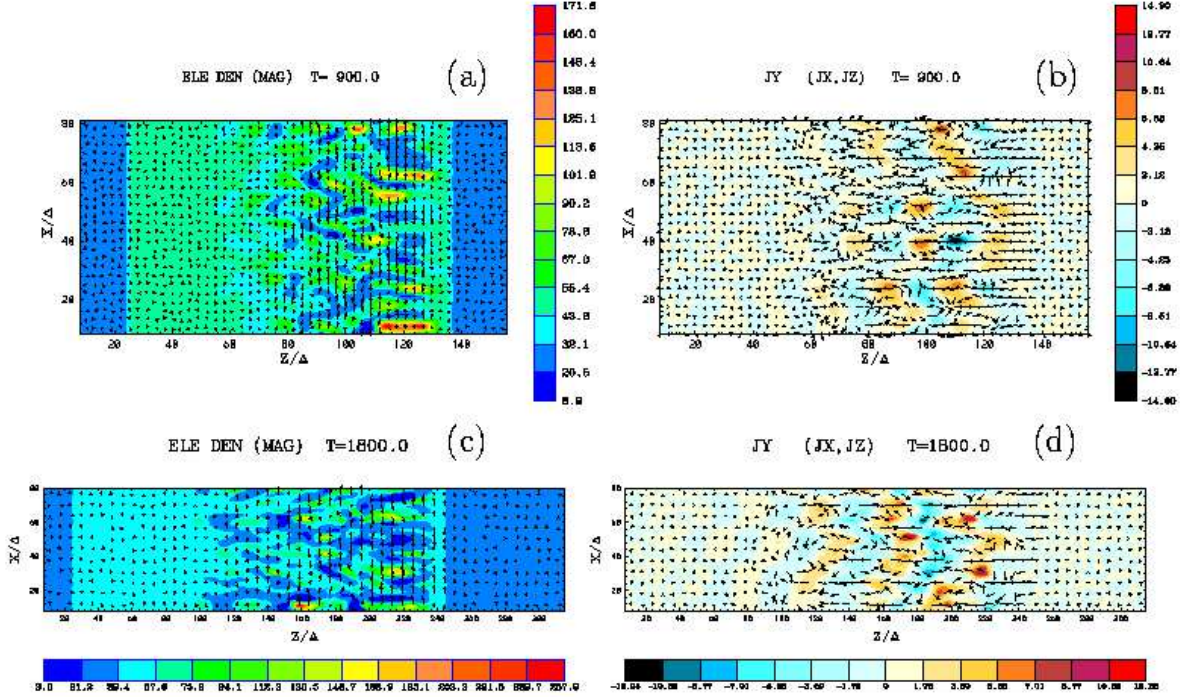


Fig. 6.— 2D images in the $x-z$ plane at $y = 43\Delta$ for a flat jet injected into an unmagnetized ambient medium shown at $t = 23.4/\omega_{pe}$. The effects of different electron skin depth are shown ((a, b): 4.8Δ ; (c, d): 9.6Δ). Due to the longer skind depth, a longer jet was simulated in (c) and (d). In (a) and (c) color indicates the electron density (peak: (a) 171.6, (c) 257.9) with magnetic fields indicated by arrows and in (b) and (d) color indicates the y -component of the current density J_y (peak: (b) 14.90, (d) 12.28), with J_z, J_x indicated by the arrows. Images (a) and (b) are comparable to images in Fig. 2 (magnetized) but the color scales are different.

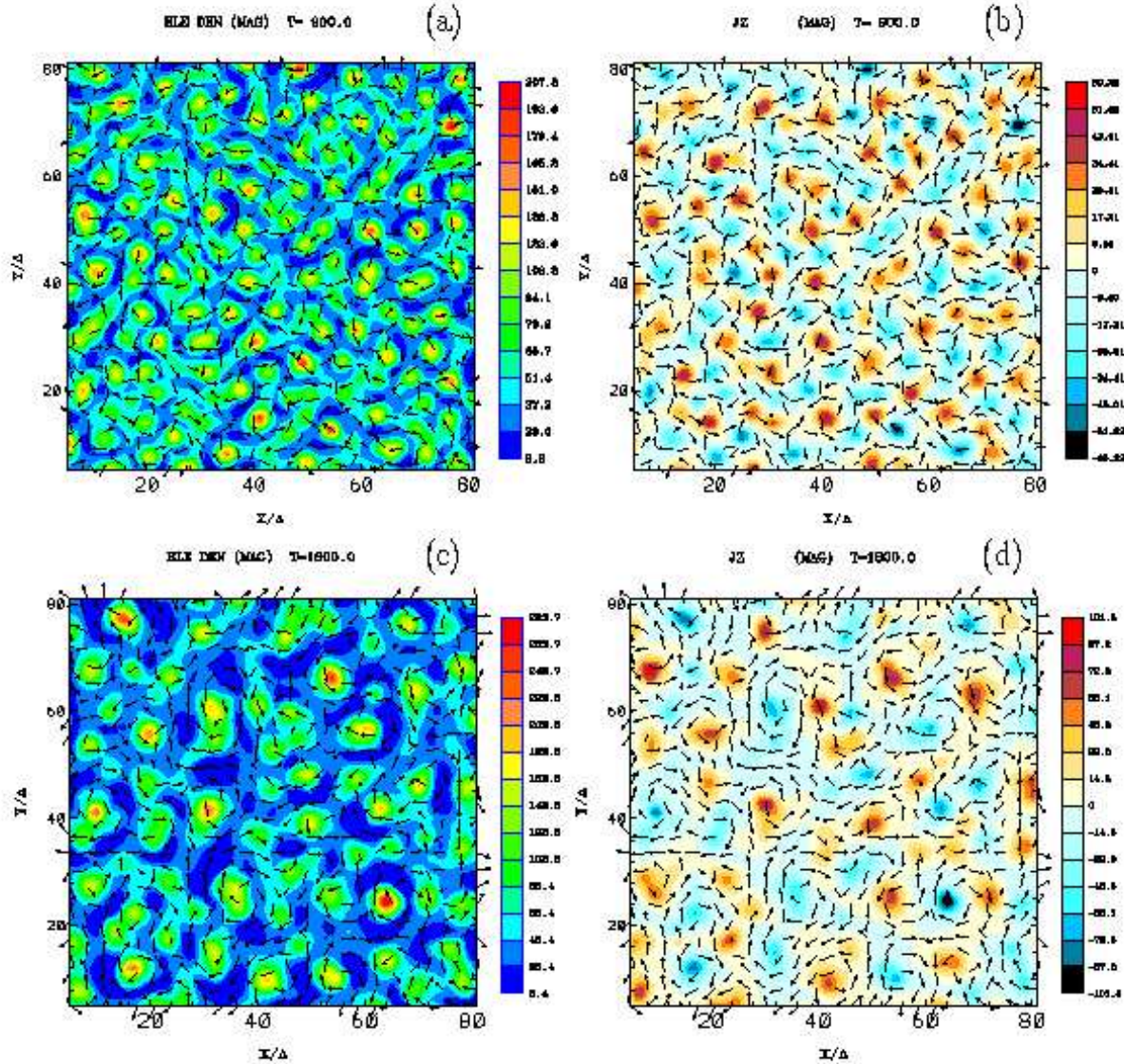


Fig. 7.— 2D images in the $x - y$ plane for a flat jet injected into an unmagnetized ambient medium at shown $t = 23.4/\omega_{pe}$. The effects of different electron skin depth are shown and as in Fig. 6 ((a, b): 4.8Δ ; (c, d): 9.6Δ). The electron density (a, c)) and z -component of the current density (b, d) are plotted at $z = 120\Delta$ (a, b) and $z = 215\Delta$ (c, d). The arrows show the transverse magnetic fields $B_{x,y}$ which are generated by J_z (in particular Fig. 7d).

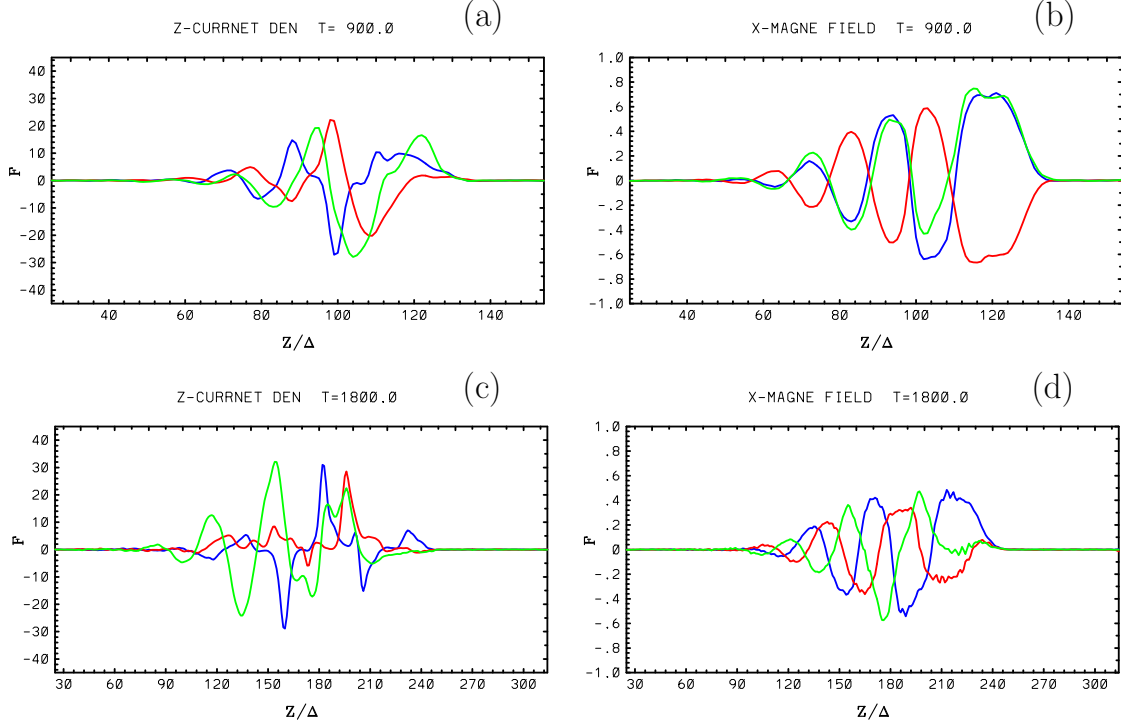


Fig. 8.— One-dimensional cuts in the z -direction of the current density (z -direction) (a, c), and the magnetic field (x -component) (b, d) shown at $t = 23.4/\omega_{pe}$. The effects of different electron skin depth are shown and as in Figs. 6 & 7 ((a, b): 4.8Δ ; (c, d): 9.6Δ). Cuts are taken at $x/\Delta = 38$ and (a, b) $y/\Delta = 38$ (blue – dotted), 43 (red – solid), 48 (green – dashed) or (c, d) $y/\Delta = 33$ (blue – dotted), 43 (red – solid), 53 (green – dashed), and are separated by about one electron skin depth.